Photochemical & Photobiological Sciences

PAPER

Cite this: *Photochem. Photobiol. Sci.*, 2019, **18**, 2421

Theoretical insights into the effect of ligands on platinum(II) complexes with a bidentate bis(*o*-carborane) ligand structure†

Ancong Zhao,[a] Wanlin Cai,[a] Xi Yan,[a] Huize Zhang,[a] Jian Wang*[b] and Wei Shen *[a]

Received 1st June 2019,
Accepted 16th July 2019

DOI: 10.1039/c9pp00251k

rsc.li/pps

Carboranes feature a wealth of unique structures and properties in phosphorescent transition-metal complexes (PTMCs). Herein, we identify the influence between the electronic structure in carboranes and the main ligand based on the density functional theory (DFT) and time-dependent density functional theory (TD-DFT), which affects the phosphorescence properties of carborane-containing Pt compounds. Furthermore, the mechanism, including singlet–triplet splitting energies $\Delta E(S_n - T_1)$, transition dipole moment for $S_0 - S_n$ transitions, the zero-field splitting (ZFS), the radiative decay rate constant (k_r), the Huang–Rhys factor (S), and the spin–orbit coupling (SOC) matrix elements $\langle T_1|H_{SOC}|S_n\rangle$ have been carefully investigated. The results presented here reveal the functional action 1,1′-bis(*o*-carborane) contributes to the emission process owing to the manipulation of main ligand dtb-bpy and complex **1a** shows promising prospects for achieving highly efficient phosphorescence *via* engineering the conjugation of the main ligand dtb-bpy.

1 Introduction

Icosahedral carboranes,[1–3] consisting of 10 boron atoms and 2 carbon atoms, show unique electronic properties and thermal stability.[4–7] Meanwhile, the self-quenching, triplet–triplet annihilation and concentration quenching in the solid state could be suppressed due to the bulkiness of organometallic complexes containing carboranes.[8–11] The phosphorescent transition-metal complexes (PTMCs) containing carboranes have attracted much interest of researchers in the past decades.[12–15] Very few Pt complexes containing carborane ligands have been reported at the current stage. The electrons in organometallic complexes containing the carborane are not distributed on the carborane,[16–19] indicating that the carborane is not participating in the emission and not related to the luminescence. Is it possible to change the electronic properties of carboranes in some way?

It is a sagacious strategy to change the coordinated ligands of organometallic complexes for obtaining high-performing OLEDs. For example, Luo *et al.* have theoretically investigated the effect of regulated main ligand π-conjugation on the photophysical properties of a series of Pt(II) NHC complexes.[20] As reported by Lu and co-workers, two cyclometalated Pt(II) complexes (TN_3T)Pt(dptp) and (4tfmppy)Pt(dptp) with high photoluminescence quantum efficiency yields were designed and synthesized through the introduction of the nitrogen atoms and CF_3 group into the main ligand.[21] Recently, the influence of different ancillary ligands on the photophysical properties of Pt(II) complexes has been theoretically researched by Wang *et al.*[22] In 2016, a series of Pt(II) complexes containing a 1,1′-bis(*o*-carborane) (denoted as bc) ligand were synthesized and characterized by A. M. Spokoyny and co-workers,[16] and they are non-emissive at room temperature. Some theoretical studies[7] have been carried out to disclose the relation between the structure and emission properties, including the different ways in which the bc ligand and Pt atom are connected as well as the number of carboranes attached to the Pt(II) center. Based on this, is it possible to adjust the electronic structure of carboranes through regulating the main ligand? What we are concerned about is that the regulation of the main ligand dtb-bpy can improve the contribution of ancillary ligand Et-bc to the molecular orbital.

Two classes of derivatives of complex **1** have been discussed. **1a**, **1a-N** (bridge atom is nitrogen atom), **1a-O** (bridge atom is oxygen atom) and **1a-PO** (bridge atom is P=O group) represent the first type which introduce the bridge atom between two pyridine groups of the dtb-bpy ligand. **1b** represents the second type which extends the conjugation length of the dtb-bpy ligand. All molecules are shown in Scheme 1.

[a]*School of Chemistry and Chemical Engineering, Southwest University, Key Laboratory of Luminescence and Real-Time Analytical Chemistry (Southwest University), Ministry of Education, Chongqing, 400715, China. E-mail: shenw@swu.edu.cn*

[b]*School of Elementary Education, Chongqing Normal University, Chongqing, 400715, China. E-mail: wangjian@cqnu.edu.cn*

†Electronic supplementary information (ESI) available. See DOI: 10.1039/c9pp00251k

Interrupting and increasing conjugation are two common ways to improve phosphorescence properties, but which one is better? To understand the photophysical properties of these compounds, the DFT[23] and TD-DFT[24–26] calculations are carried out. We believe that this preliminary work will provide valuable guidelines on designing highly efficient luminescent materials of OLEDs in the future.

2 Theoretical background

The phosphorescence quantum yield Φ_{PL} is a key parameter to study the phosphorescent materials, which usually rely on two factors: the radiative rate constant k_r and the nonradiative rate constant k_{nr} containing the temperature-independent nonradiative decay rate constant $k_{nr,1}$ and the temperature-dependent nonradiative decay rate constant $k_{nr,2}$. Their relationship can be presented as follows:

$$\Phi_{PL} = \frac{k_r}{k_r + k_{nr,1} + k_{nr,2}}. \quad (1)$$

According to eqn (1), the larger k_r and smaller k_{nr} values are beneficial for achieving high phosphorescence quantum yield (Φ_{PL}).

2.1 Radiative decay rate constant

In a non- or scalar relativistic scene, the triplet excited states get threefold degenerated. With the influence of SOC effect, the emissive triplet excited states would be split into three sublevels, and the energy differences between the sublevels are defined as the zero point splitting (ZFS) energy.[27] The radiative decay rate k_r^i and the radiative decay lifetime t_r^i from each sublevel can be presented on the basis of the perturbation theory:

$$k_r^i = \frac{1}{\tau_r^i} = k_r(S_0, T_1^i) = \frac{4\alpha_0^3}{3t_0}\Delta E_{S_0-T_{em}^i}{}^3 \sum_{j\in\{x,y,z\}} |M_j^i|^2 \quad (2)$$

where, $t_0 = \frac{(4\pi\varepsilon_0)^2\hbar^3}{m_e e^4}$, α_0 and $\Delta E_{S_0} - T_{em}^i$ refer to the fine structure constant and energy differences between T_{em} and S_0. What's more, M_j^i is the transition dipole moment of $T^i{}_{em} \rightarrow S_0$, which can be shown in the following expression:

$$M_j^i = \sum_{n=0}^{\infty} \frac{\langle S_0|\hat{\mu}_j|S_n\rangle\langle S_n|\hat{H}_{soc}|T_{em}^i\rangle}{E(S_n) - E(T_{em})} + \sum_{m=1}^{\infty} \frac{\langle S_0|\hat{H}_{soc}|T_m\rangle\langle T_m|\hat{\mu}_j|T_{em}^i\rangle}{E(T_m) - E(S_0)}. \quad (3)$$

where, $\hat{\mu}_j$ and $\hat{H}_{soc}$ represent the electron transition dipole moment as well as the spin–orbit dipole, respectively. The energy differences between S_0 and T_m are much larger than those between S_n and T_{em}, and the transition dipole moments between S_0 and S_n are much greater than those between T_m and T_{em}^i. Therefore, the latter is much smaller than the former, which could be considered as the main factor contributing to the M_j^i value. Furthermore, the distribution of the Boltzmann statistics, and the total radiative decay rate constant can be elucidated as below:

$$k^r = \frac{k_1^r + k_2^r \exp(-ZFS_{1,2}/k_B T) + k_3^r \exp(-ZFS_{1,3}/k_B T)}{1 + \exp(-ZFS_{1,2}/k_B T) + \exp(-ZFS_{1,3}/k_B T)}. \quad (4)$$

Generally speaking, both of the ZFS for transition-metal phosphors are typically less than 200 cm^{-1}.[28] Thus, at ambient temperature, eqn (4) could be broken down to:

$$k^r = \frac{1}{3}\sum_{i=1}^{3} k_i^r. \quad (5)$$

2.2 Nonradiative decay rate constant

In addition to the radiative decay rate constant, the nonradiative decay rate constant is also an important factor for the determination of phosphorescence quantum yield. On the basis of the energy-gap law,[29] the temperature-independent nonradiative decay rate constant from the T_m state to S_0 state can be expressed as follows:

$$k_{nr}(T_m \rightarrow S_0) \propto \exp\{-\beta[E(T_m) - E(S_0)]\}. \quad (6)$$

where, the nonradiative decay rate constant is closely associated with two main factors. One is the parameter β which reflects structural distortion between T_m with respect to S_0. The other is

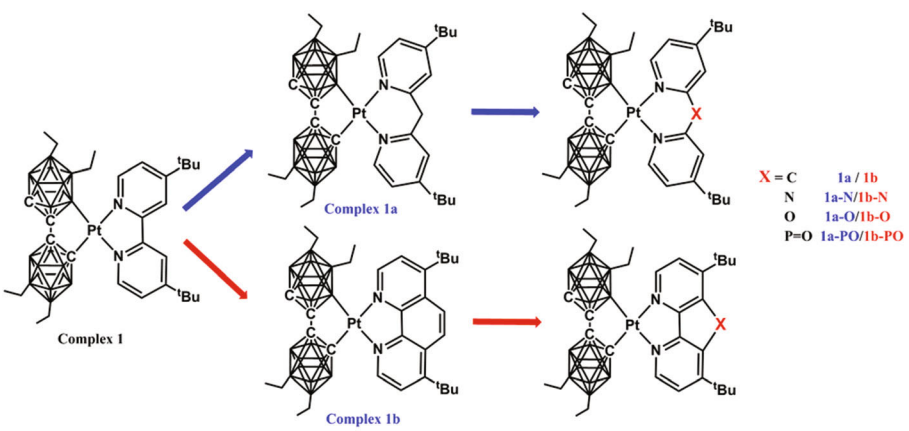

Scheme 1 Chemical structures of the two series of complexes.

the energy difference between T_m and S_0. Obviously, the larger the degree of structural distortion, the smaller the energy level difference and the faster the nonradiative inactivation process. As reported, the Huang–Rhys factors[20] of the T_1 state and S_0 state quantify the degree of molecular structural deformation. Within the displaced harmonic oscillator's approximation, the Huang–Rhys factors are described in eqn (7):

$$S = \frac{1}{2}\omega\Delta Q^2 \quad (7)$$

where S and ΔQ are the Huang–Rhys factor and the shift vector, respectively.

3 Computational details

The geometry optimizations of the ground state and the lowest-lying triplet excited state for all the studied complexes were performed by density functional theory (DFT). To find a suitable method which has good consistency with the experiment, seven different DFT methods were tested, including PBE0,[30] B3LYP,[31] BMK,[32] M052X,[33] M062X,[34] CAM-B3LYP,[35] and BP86-D3.[36–38] For the S_0 state of the experimental molecule **1**, the corresponding detailed results and the available experimental values are given in Table S1.† The results indicate that the BP86-D3 functional with the 6-31g(d) level gives a similar result to the experimental parameters, therefore, the geometry optimizations for the S_0 state and T_1 state of all complexes are employed at the level of BP86-D3. No imaginary frequency was observed, confirming the optimized geometry was at the minimum of the potential-energy surface. In addition, the metal central (^{3}MC) states, constructed through the methodology presented in Persson's work,[39] were calculated with the BP86-D3 functional. At the same time, the intrinsic reaction coordinate (IRC) was computed to confirm the reliability of the transition state.

In addition, the emission performance was studied by TD-DFT/M062X on account of the optimized T_1 geometries. All these calculations were carried out using the Gaussian 09 program package.[40] The transition metal atom Pt and light atoms (C, H, O, N, P) were calculated with the LANL2DZ basis set[41] and 6-31G (d) basis set,[42] respectively.

The radiative decay rate constant was calculated in the ADF2014.04 program package.[43] 20 lowest singlet excited states and 20 lowest triplet excited states were taken into consideration in the spin–orbit TD-DFT calculation. On the basis of the information obtained above, the phosphorescence spectra was computed using the software MOMAP.[44]

4 Results and discussion

4.1 Geometries at the ground and lowest triplet excited states

In this paper, all structures at the ground and lowest triplet excited states were calculated in the theoretical level of BP86-D3 at 6-31g (d). The structure of complex **1** as well as the related bond is labeled in Fig. 1. The main optimized structural parameters of S_0 and T_1 states for all the investigated complexes are given in Table S2.† As compared with the bond lengths in **1**, **2** exhibits significant enhancement in the ground-state for all complexes. A possible explanation is that the interaction of Pt–C is stronger than that of Pt–B. It can be easily noted that the bond lengths of Pt–C and Pt–B are smaller than those of Pt–N, indicating that the Pt atom has a stronger interaction with the carborane relative to the pyridine owing to the strong electron-withdrawing ability of the carborane. Through analyzing the bond angles of the ground-state, it suggests that the influence of interrupting and extending conjugation on the bond angles can be neglected. At the same time, by comparing the dihedral angles of the ground-state, it is not difficult to find that the dihedral angles of the **1b** series are generally reduced, while the dihedral angles of the **1a** series are different. From the results we have analyzed that it is a sagacious strategy to make the planarity better by extending the π-conjunction of the main ligands.

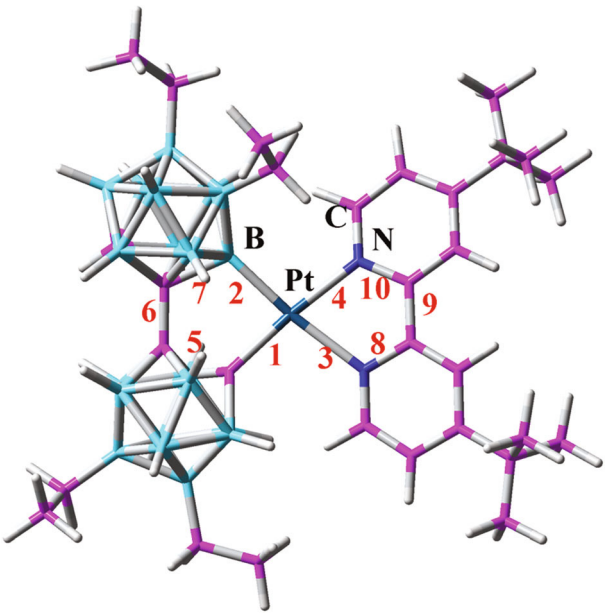

Fig. 1 Optimized geometry structures of complex **1** in the ground state.

According to the Kasha rule, the speed of ISC and IC is much faster than the phosphorescent rate. Therefore, the S_n and T_m states are more easily relaxed to the T_1 state, and the structure largely affects the radiative decay process and the non-radiative decay process.[27] The optimized geometry of T_1 is emphatically discussed. First, in comparison with the ground and lowest triplet excited states of the **1b** series, one can find that the bond lengths and bond angles have a subtle change. In addition, the T_1 state has smaller dihedral angles compared with those of the S_0 state, which demonstrates that the structural distortion is small for the **1b** series. In contrast, there is apparent structural distortion of the T_1 state for the **1a** series. Among these changes, the most obvious change is the bond angle 2–Pt–3 which is different in molecule **1a-O**, reaching 57.1°. For the dihedral angles, we have noticed a distinct vari-

ation in the **1a** series. The dihedral angle 8–9–10 of **1a-O** exhibits significant changes (18.02°) between the S_0 state and the T_1 state. In order to more accurately describe the degree of structural distortion between the S_0 state and the T_1 state, the root mean square difference (RMSD) was calculated using the VMD 1.9 program.[45] As we guessed, the RMSD of the molecule **1a-O** (2.153) is larger than others, that is to say the structural distortion is the largest between the S_0 state and T_1 state in the molecule **1a-O**. Importantly, the RMSD of the **1b** series is smaller than that of complex **1**, while that of the **1a** series is larger than that of complex **1**, indicating that the T_1 state of the **1a** series is greatly distorted which may lead to a larger nonradiative rate constant.

4.2 Phosphorescence properties

On the basis of the T_1 state, calculated vertical transition energy (ΔE_{vert}) configuration, characteristics, and available experimental emission maxima are given in Table 1. The TD-DFT calculations are consistent with the experimental value, which proves the credibility of the method we chose. Furthermore, the molecular orbital character of the T_1 state is shown in Table S4.† The lowest-energy emission of complex **1** is mainly ascribed to the transition from HOMO−1 to LUMO. The lowest-energy emission of the **1b** series, which is the electronic transition property corresponding to the maximum emission wavelength, is primarily attributed to the transition from HOMO−1 character to LUMO character. However, the emission process of the **1a** series shows a remarkable difference. The electronic transition properties corresponding to their maximum emission wavelengths are chiefly attributed to their transition from the HOMO to the LUMO. The results presented here reveal that the interruption of conjugation shows a marked difference for molecular character, while the extension of the conjugation has no effect on the transition properties.

Table 1 The calculated triplet emissive wavelength (nm), and transition character for studied complexes together with the experimental values

	ΔE_{vert}	Configuration	Character	E_{exp}
1	498	H−1 → L (48%)	MLCT/ILCT/LLCT	497
		H−5 → L (21%)	ILCT/LLCT	
1a	842	H → L (56%)	MLCT/ILCT/LLCT	
		H → L+3 (12%)	MLCT/ILCT/LLCT	
		H → L+4 (10%)	MLCT/ILCT/LLCT	
1a-N	436	H → L (72%)	MLCT/ILCT/LLCT	
		H−1 → L (11%)	MLCT/ILCT/LLCT	
1a-O	1015	H → L (69%)	MLCT/ILCT/LLCT	
		H → L+2 (11%)	MLCT/ILCT/LLCT	
1a-PO	640	H → L (60%)	MLCT/ILCT/LLCT	
		H → L+4 (15%)	MLCT/ILCT/LLCT	
1b	513	H−1 → L (75%)	MLCT/ILCT/LLCT	
1b-N	459	H−1 → L (56%)	MLCT/ILCT/LLCT	
		H → L (19%)	MLCT/LLCT	
1b-O	460	H → L (24%)	MLCT/LLCT	
		H−1 → L (43%)	MLCT/ILCT/LLCT	
		H−5 → L (17%)	ILCT/LLCT	
1b-PO	501	H−1 → L (37%)	MLCT/ILCT/LLCT	
		H−5 → L (37%)	MLCT/ILCT/LLCT	
		H−6 → L (14%)	MLCT/ILCT/LLCT	

Strictly speaking, it is imprecise to describe the transition properties through the data in Table 1, because more than one configuration of transition could be included. To shed light on the phosphorescence properties, the natural transition orbitals (NTOs) were calculated based on the T_1 state, which is shown in Fig. 2. The "hole" represents the occupied NTOs, while the "electron" refers to the unoccupied NTOs. For the **1b** series, the electron NTOs are distributed over the metal center and dtb-bpy ligand, whereas the hole NTOs are predominantly located on the metal center and partially on the ancillary. The key point of the NTO distribution is similar to molecule **1**, which means that extending the conjugation of the main ligand does not change the molecular transition properties. In comparison with complex **1**, the hole and electron NTOs of the **1a** series have obvious differences, and the hole NTOs are obviously distributed from the metal center to the ancillary ligand (Et-bc ligand); the reason for this may be that the carborane is involved in the transition process. In the meantime, it is a rare phenomenon for carborane which is participating in the transition process. Additionally, it is worth noting that the reduction of the proportion of metals in holes makes the reduction of the transition nature defined as MLCT[46] in the **1a** series correspondingly, which could affect the radiative inactivation process.

With the development of computational chemistry, it is convenient to compute the phosphorescence spectra, which are helpful in understanding the phosphorescence properties of transition-metal complexes.[47] The calculated room-temperature optical emission spectra of complex **1** are shown in Fig. 3. The theoretical phosphorescence emission spectra agree well with the experimental line shapes, which confirm the reliability of the TVCF formalism adopted in this work. Compared to the parent compounds, the interruption of conjugation exhibits red-shifted emission bands. The serious structural distortions for the **1a** series and **1a** class are not listed. The emission band would be broadened for organometallic compounds with higher total Huang–Rhys factors, especially when the temperatures increase. The Huang–Rhys factors are discussed in section 4.4.

4.3 The radiative decay process

High phosphorescence quantum yields often require a large radiative rate constant k_r and a small nonradiative rate constant k_{nr}, simultaneously. In this way, the radiative decay process plays an important role in the molecular photophysical properties. On the basis of perturbation theory, the radiative rate constant is calculated together with the available data in the experiment as shown in Table 2. As shown, the calculated radiative rate constant of molecule **1** is similar to those of the experimental value, indicating the feasibility of the method we chose, while for the **1b** series, the calculated radiative rate constant elucidates that the prolongation of the conjugation chain has little influence on the radiative decay process. What is surprising is the reduction of the radiative rate constant (**1b-PO**), which may be caused by the strong electron-withdrawing properties of the phosphoryl group. At the same time, the k_r value of **1a** is nearly an order of magnitude smaller

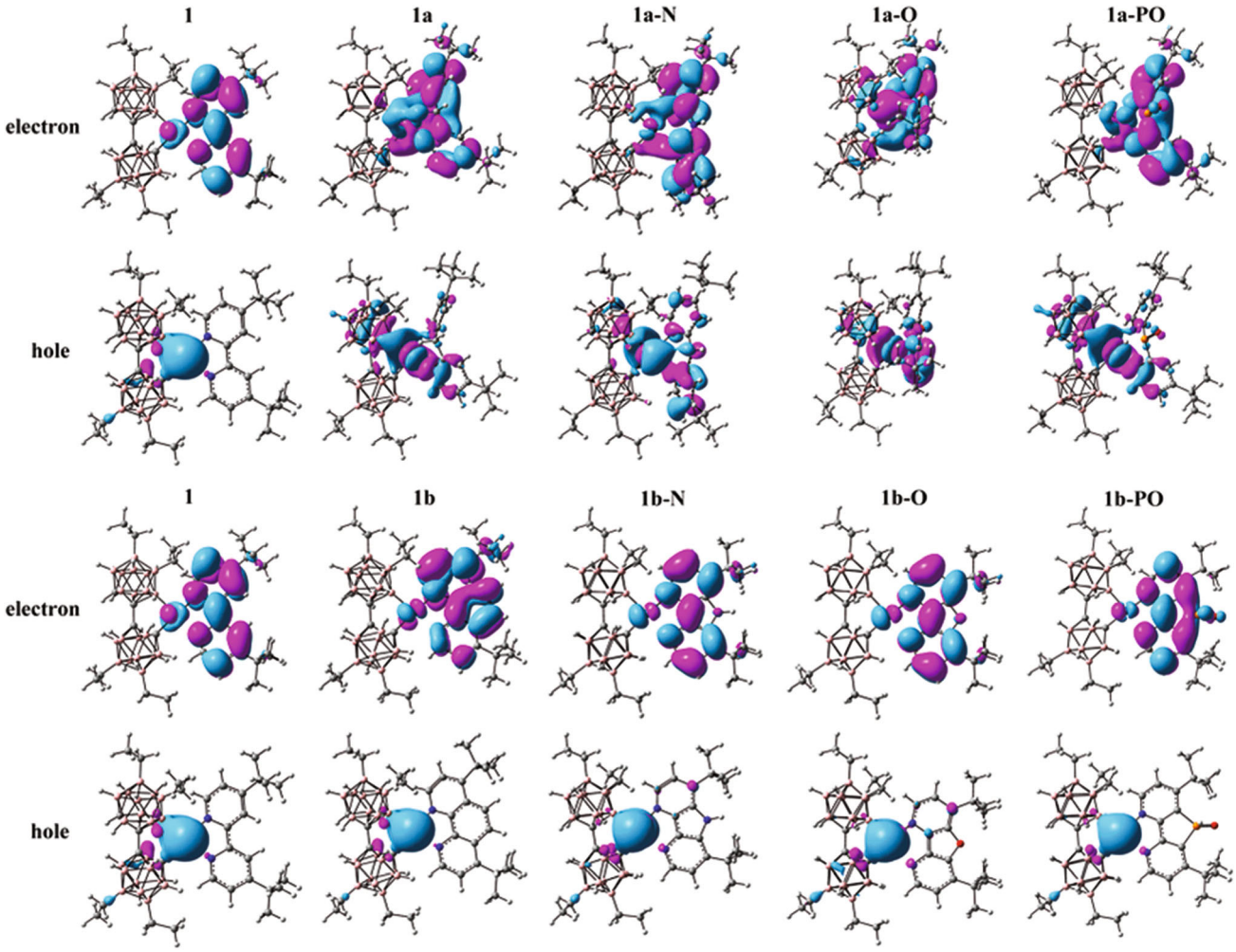

Fig. 2 NTO pairs calculated at the excited T_1 state for the two classes of complexes.

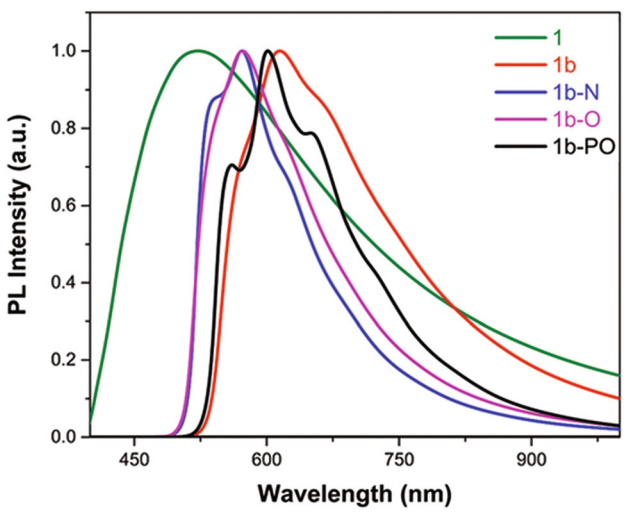

Fig. 3 Calculated optical emission spectra for complex **1** and the **1b** class.

than that of molecule **1**, manifesting that the disruption of conjugation has a greater influence on the radiative deactivation process. The molecule **1a-N** and **1b-N** have the largest radiation rate constant and may have a higher phosphorescence quantum yield. We will discuss the factors affecting the radiation deactivation process from several aspects.

The zero field splitting (ZFS) is a crucial parameter which assesses the radiative decay rate. Given the SOC effect, the T_1 state could split into three sub-levels. The stronger the SOC effect, the larger the ZFS values. This could result in a large radiative rate constant (or short radiative lifetime). Owing to the reduction of ZFS, the radiative rate constant of the **1a** class (except for **1a-N**) is much lower than that of complex **1**, as shown in Table 2. There is a tiny difference in ZFS for the **1b** class (except for **1b-PO**) with respect to **1**. However, the k_r values of molecules **1a-N** and **1b-PO** are exceptional. Therefore, ZFS does not fully control the magnitude of the radiative rate constant, and the other factors need to be discussed.

M_j^i, which is also a key factor for influencing the radiative decay rate, contains all information on the transition dipole moments μ_j, singlet–triplet splitting energies $\Delta E(S_n - T_1)$, and

Table 2 Radiative decay rate constants k_r (s^{-1}), ZFS parameters (cm^{-1}) and radiative decay lifetime τ_r (μs) for the studied complexes together with the available experimental values

	1	1a	1a-N	1a-O	1a-PO
k_r [a] (Exp.)	1.67×10^4				
k_r	1.76×10^4	2.9×10^3	2.25×10^4	9.63×10^3	4.53×10^3
ZFS	175.4	50.65	117.68	37.83	49.93
τ_r	5.67×10^{-5}	3.44×10^{-4}	4.44×10^{-5}	1.04×10^{-4}	2.36×10^{-4}

	1b	1b-N	1b-O	1b-PO
k_r	1.25×10^4	3.05×10^4	2.71×10^4	2.60×10^3
ZFS	301.40	225.83	204.62	122.51
τ_r	7.98×10^{-5}	3.28×10^{-5}	3.69×10^{-4}	3.85×10^{-4}

[a] Available experimental values from ref. 16.

Table 3 Transition dipole moments μ_j (Debye) for S_0–S_n transitions, singlet–triplet splitting energies $\Delta E(S_n - T_1)$ (eV) and the SOC matrix elements $\langle T_1|H_{SOC}|S_n\rangle$ (cm^{-1}) of complexes

	S_n	μ_j	$\Delta E(S_n - T_1)$	H_{SOC}		S_n	μ_j	$\Delta E(S_n - T_1)$	H_{SOC}
1	S_2	0.18	0.42	1629					
	S_3	1.52	0.80	1444					
	S_4	0.89	1.17	313					
1a	S_5	0.47	1.63	1393	**1b**	S_3	0.38	0.44	1617
	S_6	0.59	1.73	422		S_5	1.42	0.75	1306
	S_7	0.17	1.83	1140		S_6	1.59	1.05	517
1a-N	S_2	0.29	0.35	1449	**1b-N**	S_2	0.47	0.44	1621
	S_3	0.35	0.61	1173		S_3	2.14	0.81	1417
	S_4	0.78	0.67	747		S_9	1.79	1.54	378
1a-O	S_4	0.32	1.40	1372	**1b-O**	S_2	0.49	0.44	1606
	S_5	1.20	1.62	719		S_3	2.07	0.78	1416
	S_6	1.17	1.72	1136		S_{10}	0.14	1.62	264
1a-PO	S_5	0.50	1.37	1360	**1b-PO**	S_2	0.11	0.40	1632
	S_6	0.25	1.61	1088		S_3	1.23	0.73	1399
	S_9	0.48	2.02	365		S_4	0.57	0.77	429

the SOC matrix elements $\langle T_1|H_{SOC}|S_n\rangle$. For the investigated complexes, the three largest $\langle T_1|H_{SOC}|S_n\rangle$ values are given in Table 3 and more detailed information can be seen in Table S5.† Meanwhile, the larger the spin–orbit coupling interaction between T_1 and S_n states, the faster the process of radiative decay. As shown in Table 2, the reason for similar values of k_r in the **1b** series could be ascribed as the approximation SOC matrix elements and the singlet–triplet splitting energies (ΔE); while for **1b-PO**, reduced radiative decay behavior relative to others may be caused by the smaller μ_j. On comparing with complex **1**, the k_r values of the molecule **1a** class are found to be significantly decreased due to the much larger splitting energies $\Delta E(S_n - T_1)$. However, the molecule **1a-N** is exceptional, which may be due to the small splitting energy. All in all, the intrinsic factors of k_r can be effectually tuned by interrupting and increasing conjugation.

4.4 Temperature-independent nonradiative decay

In accordance with the energy-gap law, both the energy gap between T_1 and S_0 and structural distortion are two important aspects effecting the temperature-independent nonradiative decay. In this paper, the maximum Huang–Rhys factor (S_{max}) and RMSD quantitatively reflect the degree of molecular deformation. The calculated results and the experimental data are given in Table 4. Considering that the Huang–Rhys factor S is smaller than **1**, the structural distortion could be ignored. On account of the serious structural distortion, the calculated Huang–Rhys factor may be not precise, and the **1a** class is not given in Table 4. As shown, the molecular planarity and rigidity could be improved on the condition of extending the

Table 4 the energy differences between T_1 and S_0 states $\Delta E_{T_1-S_0}$ (kcal mol^{-1}), SOC matrix elements $\langle T_1|\hat{H}_{SOC}|S_0\rangle$ (cm^{-1}), RMSD and Huang–Rhys factor S_M together with the available experimental values

	1	1a	1a-N	1a-O	1a-PO
k_{nr} [a] (Exp.)	2.21×10^{-5}				
ΔE_{T1-S0}	57.5	60.9	60.4	61.7	61.4
$\langle T_1|H_{SOC}|S_0\rangle$	535	238	234	115	245
RMSD	0.329	0.705	0.915	2.153	1.011
S_M	6.41				

	1b	1b-N	1b-O	1b-PO
$\Delta E_{T_1-S_0}$	55.8	57.3	58.0	55.4
$\langle T_1|H_{SOC}|S_0\rangle$	571	580	556	446
RMSD	0.103	0.075	0.077	0.056
S_M	0.77	0.40	0.55	0.97

[a] Available experimental values from ref. 16.

conjugation due to the smaller structural distortion and Huang–Rhys factor in the **1b** class. In addition, the RMSD of the **1b** series is smaller than that of molecule **1**, while the RMSD of the **1a** series is bigger than that of **1**. That is coincident with the deduction mentioned above.

Another key factor which influences the process of nonradiative decay is that energy gap $E(T_1) - E(S_0)$. The larger the energy gap $E(T_1) - E(S_0)$, the slower the process of nonradiative decay. For the **1a** series, $\Delta E(T_1 - S_0)$ is larger than that of complex **1**, demonstrating that interrupting the conjugation could prompt the splitting of S_0 and T_1 states and the reduction of nonradiative decay. As compared with the **1b** series, the energy gap $E(T_1) - E(S_0)$ has no distinct difference comparable to that of molecule **1**, and only the tiny differences are embodied through extending the conjugation. In this way, there is no marked difference in the nonradiative decay.

In addition, the SOC matrix elements from the lowest-lying triplet excited state to the ground state also play an important part in reflecting the temperature-independent nonradiative decay process on the basis of the theory which is put forward by Chi-Ming Che[48] and Prof. Che.[49] As shown, the values of the SOC matrix elements between S_0 and T_1 states for all the designed **1a** series are smaller than those of complex **1**, concluding that the interrupting conjugation through introducing bridging atoms between two pyridine ligands in the dtb-bpy ligand could reduce the values of $\langle T_1|\hat{H}_{SOC}|S_0\rangle$; it may be beneficial for prohibiting the temperature-independent nonradiative decay process. In contrast, the values of the SOC matrix element have no significant difference in the **1b** series, disclosing that increasing conjugation has no apparent difference for the temperature-independent nonradiative process.

To sum up, interrupting conjugation not only reduces the values of $\langle T_1|\hat{H}_{SOC}|S_0\rangle$, but also obviously increases the values of energy gap $E(T_1) - E(S_0)$. The temperature-independent nonradiative decay rate is distinctly reduced through the interruption of conjugation, which ascertains that the nonradiative decay rates of the **1a** series may be smaller than complex **1**. The same tendency of the **1b** series and complex **1**, the energy gap $E(T_1) - E(S_0)$ and the values of $\langle T_1|\hat{H}_{SOC}|S_0\rangle$, can be observed.

4.5 Temperature-dependent nonradiative decay

There is a possibility for the triplet state to rapidly convert from the ^{3}MLCT state to the ^{3}MC state; there is a path by which the ^{3}MC state would be back to the S_0 state *via* nonradiative decay through MECP. This conversion is very fast and irreversible. Therefore, the population of the ^{3}MC state is one of the important parts for determining $k_{nr}(T)$. To further explore the process, the potential energy curve of the deactivation pathway is built, which is shown in Scheme 2. The following key points, *i.e.*, ^{1}GS state, ^{3}ES state, ^{3}MC state, TS state and the MECP of ^{3}MC/^{1}GS, are first determined. Then, these key points are connected by curves on the grounds of their respective relative energy values, which are given in Table 5. The distorted geometries of the ^{3}MC state are established by extending the metal–ligand bond length on the basis of the optimized S_0 geometries. The ^{3}MC states for all the

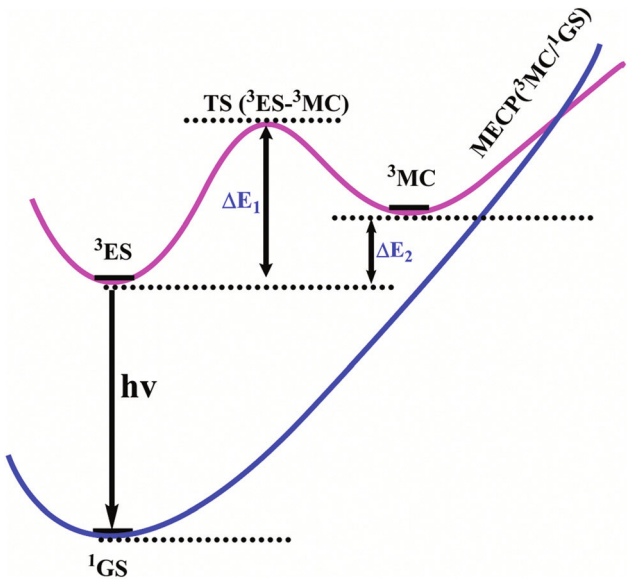

Scheme 2 The potential energy curves of thermal decay channels.

Table 5 The activation barriers (kcal mol^{-1}), ΔE_1 (^{3}ES → ^{3}TS), ΔE_2 (^{3}ES → ^{3}MC), for the nonradiative thermal deactivation process for these 2 classes of complexes

	1	**1a**	**1a-N**	**1a-O**	**1a-PO**
ΔE_1	1.70	4.77	2.49	3.03	
ΔE_2	−6.47	1.24	−5.29	−5.54	1.70
	1b	**1b-N**	**1b-O**	**1b-PO**	
ΔE_1	2.46	4.06	1.88		
ΔE_2	−4.12	−3.30	−4.02	−2.92	

studied compounds with the spin density are depicted in Fig. 4. The greatly distorted geometric structures and the spin density are mainly focused on the metal atom, which is in good accordance with the ^{3}MC state. For compound **1**, the energy of the ^{3}MC state is lower than that of the ^{3}ES state, manifesting that the conversion[50] is a spontaneous process from the ^{3}ES state to the ^{3}MC state. The barrier energy ΔE_1 of complex **1** is only 1.70 kcal mol^{-1} and the exothermic energy ($\Delta E_1 - \Delta E_2$) is 8.44 kcal mol^{-1}. For complex **1**, it is not difficult to overcome these barriers and radiate to the ground state with increasing temperature; that is why complex **1** could emit blue phosphorescence at 77 K but be non-emissive at indoor temperature. The ^{3}ES state to ^{3}MC conversion would be impeded on the condition of a high enough activation barrier; the temperature-dependent nonradiative deactivation process can be suppressed.

As shown in Table 5, the barrier has changed by extending the conjugation of the dtb-bpy ligand in comparison to complex **1**. For the **1b** class, the absolute value of ΔE_2 decreases obviously, indicating that it is difficult to directly inactivate the complex **1b** series from the ^{3}MC state to the S_0 state. Among them, **1b-N** has the largest ΔE_1 value, which means that the ^{3}ES state → ^{3}MC state conversion has the

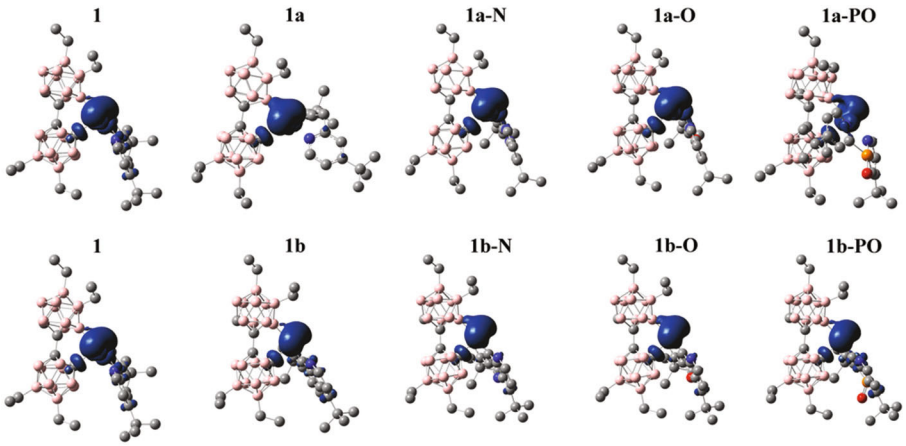

Fig. 4 Spin density distribution computed at the ^{3}MC state for all the studied complexes (isovalue = 0.004).

highest energy barrier and it is difficult to convert from the ^{3}ES state to ^{3}MC state. In the **1b** series, the temperature-dependent nonradiative rate constant of **1b-N** may be minimum. Compared with complex **1**, **1a** possesses prominent energy barrier changes. Furthermore, the energy barrier ΔE_2 with the positive reaction energy of complex **1a** reflecting the conversion from the ^{3}ES state to the ^{3}MC state is not a spontaneous process any more. Owing to the positive energy gap and the largest energy differences (ΔE_2), there is obvious reduction for the temperature dependent nonradiative rate.

On the whole, the regulation of the dtb-bpy ligand can effectively improve the nonradiative inactivation process and the **1a** complex may have the slowest nonradiative process due to its maximum energy barrier. Additionally, it may have a nonradiative rate constant similar to that at low temperatures in comparison to room temperature.

5 Conclusion

In conclusion, DFT/TDDFT methods have been successfully employed in the study of electronic structures, phosphorescence properties, and radiative and nonradiative decay processes of Pt(II) complexes with the bidentate 1,1′-bis(*o*-carborane). These results obtained indicate that breaking or extending the conjugation of the main ligand strikingly influences the properties of the compound. It's worth noting that the regulation of the main ligand dtb-bpy can improve the contribution of the ancillary ligand Et-bc to the molecular orbital; it makes the 1,1′-bis(*o*-carborane) ligand the functional ligand. For modulating the phosphorescence properties, interrupting conjugation is more suitable in comparison with extending conjugation.

1a, with a higher phosphorescence quantum yield, may be a promising phosphorescence compound for high-efficiency OLEDs by analyzing the radiative rate constants, the nonradiative deactivation process and so on. In conclusion, the reasonable regulation of Pt(II) complexes with a 1,1′-bis(*o*-carborane) ligand will provide a sagacious strategy for further designing high-performance luminescent materials applied in OLEDs.

Conflicts of interest

There are no conflicts to declare.

Acknowledgements

This work was funded by the Chongqing Research Program of Basic Research and Frontier Technology (No. cstc2018jcyjAX0004).

References

1 T. L. Heying, J. W. Ager Jr., S. L. Clark, D. J. Mangold, H. L. Goldstein, M. Hillman, R. J. Polak and J. W. Szymanski, *Inorg. Chem.*, 1963, **2**, 1089–1092.
2 M. M. Fein, J. Bobinski, N. Mayes, N. Schwartz and M. S. Cohen, *Inorg. Chem.*, 1963, **2**, 1111–1115.
3 M. M. Fein, D. Grafsteinn, J. E. Paustian, J. Bobinski, B. M. Lichstein, N. Mayes and M. S. Cohen, *Inorg. Chem.*, 1963, **2**, 1115–1119.
4 X. Li, H. Yan and Q. Zhao, *Chem. – Eur. J.*, 2016, **22**, 1888–1898.
5 H. Zhang, W. Li, X. Yan, W. Cai, M. Li, R. He and W. Shen, *New J. Chem.*, 2018, **42**, 5955–5966.
6 H. Naito, Y. Morisaki and Y. Chujo, *Angew. Chem., Int. Ed.*, 2015, **54**, 5084–5087.
7 W. Li, X. Yan, H. Zhang, R. He, M. Li and W. Shen, *Eur. J. Inorg. Chem.*, 2018, **2018**, 99–108.
8 A. M. Prokhorov, T. Hofbeck, R. Czerwieniec, A. F. Suleymanova, D. N. Kozhevnikov and H. Yersin, *J. Am. Chem. Soc.*, 2014, **136**, 9637–9642.

9 A. Ferrer-Ugalde, J. Cabrera-Gonzalez, E. J. Juarez-Perez, F. Teixidor, E. Perez-Inestrosa, J. M. Montenegro, R. Sillanpaa, M. Haukka and R. Nunez, *Dalton Trans.*, 2017, **46**, 2091–2104.

10 K. Nishino, K. Uemura, K. Tanaka and Y. Chujo, *New J. Chem.*, 2018, **42**, 4210–4214.

11 H. Naito, K. Uemura, Y. Morisaki, K. Tanaka and Y. Chujo, *Eur. J. Inorg. Chem.*, 2018, **2018**, 1885–1890.

12 C. Shi, H. Sun, X. Tang, W. Lv, H. Yan, Q. Zhao, J. Wang and W. Huang, *Angew. Chem., Int. Ed.*, 2013, **52**, 13434–13438.

13 H. J. Bae, J. Chung, H. Kim, J. Park, K. M. Lee, T. W. Koh, Y. S. Lee, S. Yoo, Y. Do and M. H. Lee, *Inorg. Chem.*, 2014, **53**, 128–138.

14 M. Tominaga, H. Naito, Y. Morisaki and Y. Chujo, *New J. Chem.*, 2014, **38**, 5686–5690.

15 Y. Kim, S. Park, Y. H. Lee, J. Jung, S. Yoo and M. H. Lee, *Inorg. Chem.*, 2016, **55**, 909–917.

16 K. O. Kirlikovali, J. C. Axtell, A. Gonzalez, A. C. Phung, S. I. Khan and A. M. Spokoyny, *Chem. Sci.*, 2016, **7**, 5132–5138.

17 J. C. Axtell, K. O. Kirlikovali, P. I. Djurovich, D. Jung, V. T. Nguyen, B. Munekiyo, A. T. Royappa, A. L. Rheingold and A. M. Spokoyny, *J. Am. Chem. Soc.*, 2016, **138**, 15758–15765.

18 L. Boehling, A. Brockhinke, J. Kahlert, L. Weber, R. A. Harder, D. S. Yufit, J. A. K. Howard, J. A. H. MacBride and M. A. Fox, *Eur. J. Inorg. Chem.*, 2016, **2016**, 403–412.

19 X. Li, H. Yan and Q. Zhao, *Chem. – Eur. J.*, 2016, **22**, 1888–1898.

20 Y. Luo, Y. Xu, W. Zhang, W. Li, M. Li, R. He and W. Shen, *J. Phys. Chem. C*, 2016, **120**, 3462–3471.

21 G. Z. Lu, Z. L. Tu, L. Liu, Y. X. Zheng and Y. Zhao, *Dalton Trans.*, 2019, **48**, 1892–1899.

22 X. Wang, J. Zhang, X. Zhu, T. Ren and L. Wang, *Spectrochim. Acta, Part A*, 2018, **204**, 340–347.

23 A. D. Becke, *J. Chem. Phys.*, 2014, **140**, 18A301–18A501.

24 J. G. Snijders, E. J. Baerends and P. Ros, *Mol. Phys.*, 1979, **38**, 1909–1929.

25 J. Autschbach, T. Ziegler, S. J. A. van Gisbergen and E. J. Baerends, *J. Chem. Phys.*, 2002, **116**, 6930–6940.

26 Y. L. Li, L. Han, Y. Mei and J. Z. H. Zhang, *Chem. Phys. Lett.*, 2009, **482**, 217–222.

27 S. W. Lai and C. M. Che, *Top. Curr. Chem.*, 2004, **241**, 27–63.

28 H. Yersin, A. F. Rausch, R. Czerwieniec, T. Hofbeck and T. Fischer, *Coord. Chem. Rev.*, 2011, **255**, 2622–2652.

29 N. C. Joanne, S. Wilson, M. R. A. Al-Mandhary, M. Younus, M. S. Khan, P. R. Raithby and R. H. Friend, *J. Am. Chem. Soc.*, 2001, **123**, 9412–9417.

30 Y. Zhao and D. G. Truhlar, *J. Chem. Phys.*, 2006, **125**, 194101–194103.

31 S. L. Mayo, B. D. Olafson and W. A. Goddard, *J. Phys. Chem.*, 1990, **94**, 8897–8909.

32 A. D. Boese and J. M. Martin, *J. Chem. Phys.*, 2004, **121**, 3405–3416.

33 E. G. Hohenstein, S. T. Chill and C. D. Sherrill, *J. Chem. Theory Comput.*, 2008, **4**, 1996–2000.

34 Y. Zhao and D. G. Truhlar, *Theor. Chem. Acc.*, 2007, **120**, 215–241.

35 T. Yanai, D. P. Tew and N. C. Handy, *Chem. Phys. Lett.*, 2004, **393**, 51–57.

36 A. D. Becke, *Phys. Rev. A*, 1988, **38**, 3098–3100.

37 J. P. Perdew, *Phys. Rev. B: Condens. Matter Mater. Phys.*, 1986, **33**, 8822–8824.

38 S. Grimme, S. Ehrlich and L. Goerigk, *J. Comput. Chem.*, 2011, **32**, 1456–1465.

39 M. Abrahamsson, M. J. Lundqvist, H. Wolpher, O. Johansson, L. Eriksson, J. Bergquist, T. Rasmussen, H. C. Becker, L. Hammarstrom, P. O. Norrby, B. Akermark and P. Persson, *Inorg. Chem.*, 2008, **47**, 3540–3548.

40 M. J. Frisch, G. W. Trucks, H. B. Schlegel, G. E. Scuseria, M. A. Robb, J. R. Cheeseman, G. Scalmani, V. Barone, G. A. Petersson, *et al.*, *Gaussian 09, Revision D.01*, Gaussian, Inc., Wallingford, CT, 2013.

41 P. J. Hay and W. R. Wadt, *J. Chem. Phys.*, 1985, **82**, 299–310.

42 P. C. Hariharan and J. A. Pople, *Mol. Phys.*, 2006, **27**, 209–214.

43 C. F. Guerra, J. G. Snijders, G. te Velde and E. J. Baerends, *Theor. Chem. Acc.*, 1998, **99**, 391–403.

44 Y. Niu, W. Li, Q. Peng, H. Geng, Y. Yi, L. Wang, G. Nan, D. Wang and Z. Shuai, *Mol. Phys.*, 2018, **116**, 1078–1090.

45 K. L. Bak and P. Jorgensen, *J. Chem. Phys.*, 1993, **98**, 8873–8887.

46 S. Y. Chang, J. Kavitha, S. W. Li, C. S. Hsu, Y. Chi, Y. S. Yeh, P. T. Chou, G. H. Lee, A. J. Carty, Y. T. Tao and C. H. Chien, *Inorg. Chem.*, 2006, **45**, 137–146.

47 W. Cai, H. Zhang, X. Yan, A. Zhao, R. He, M. Li, Q. Meng and W. Shen, *Phys. Chem. Chem. Phys.*, 2019, **21**, 8073–8080.

48 G. S. Ming Tong, K. T. Chan, X. Chang and C. M. Che, *Chem. Sci.*, 2015, **6**, 3026–3037.

49 G. S. Tong, P. K. Chow, W. P. To, W. M. Kwok and C. M. Che, *Chem.*, 2014, **20**, 6433–6443.

50 W. H. Lam, E. S. H. Lam and V. W. W. Yam, *J. Am. Chem. Soc.*, 2013, **135**, 15135–15143.